JOURNAL OF GEOPHYSICAL RESEARCH: SPACE PHYSICS, VOL. 118, 1–13, doi:10.1002/jgra.50296, 2013

ARTEMIS observations of lunar dayside plasma in the terrestrial magnetotail lobe

Y. Harada,[1] S. Machida,[1] J. S. Halekas,[2] A. R. Poppe,[2] and J. P. McFadden[2]

Received 7 February 2013; revised 19 April 2013; accepted 23 April 2013.

[1] We report observations by the dual-probe Acceleration, Reconnection, Turbulence and Electrodynamics of the Moon's Interaction with the Sun (ARTEMIS) mission of Moon-related electron and ion signatures obtained above the dayside lunar surface in the terrestrial magnetotail lobes. While the Moon is often thought of as a passive absorber, recent observations from Kaguya, Chandrayaan, Chang'E, and ARTEMIS indicate that plasma of lunar origin can have significant effects on the near-lunar environment. We now present new observations from ARTEMIS showing that lunar plasma can play a dominant role in the low-density environment of the terrestrial magnetotail. Two-point observations reveal that the density of plasma of lunar origin is higher than that of the ambient lobe plasma even several hundreds of kilometers above the Moon's dayside. Meanwhile, the distributions of incoming electrons exhibit modifications correlated with Moon-related populations, suggesting direct or indirect interactions of the lobe electrons with plasma of lunar origin. We also observe high-energy photoelectron emission from the dayside lunar surface, supporting the existence of large positive potentials on the lunar surface. Pickup ions with nonzero parallel-velocity components provide further evidence for positive surface potentials of tens of volts or more. ARTEMIS data reveal not only the existence of the positive surface potentials much larger than those predicted from a current-balance model based on Maxwellian plasmas but also their significant implications for the dynamics of both the dominant Moon-originating ions and the tenuous ambient plasma populations in the tail lobe.

Citation: Harada, Y., S. Machida, J. S. Halekas, A. R. Poppe, and J. P. McFadden (2013), ARTEMIS observations of lunar dayside plasma in the terrestrial magnetotail lobe, *J. Geophys. Res. Space Physics*, *118*, doi:10.1002/jgra.50296.

1. Introduction

[2] The lack of both a thick atmosphere and an intrinsic magnetic field causes direct interactions between the Moon and its ambient plasma. Plasma interactions with the Moon, including its remanent magnetic fields, significantly modify the electron- and ion-velocity distribution functions through various processes, such as absorption, acceleration, reflection, and scattering of charged particles. Direct interactions of the lunar surface with the plasma give rise to an important process, namely surface charging. The electrostatic potential of the lunar surface strongly depends on the ambient plasma conditions [*Halekas et al.*, 2008].

[3] Charging mechanisms of an airless body in space have been studied for decades, specifically with the aim of preventing spacecraft malfunctions attributed to surface charging and electrostatic discharges [*Whipple*, 1981]. Bombardment of incident charged particles, as well as photoelectron emission caused by incident high-energy photons, results in charge transfer between the surface and space. The charged particles are attracted or repelled by the electric field generated by the charge that has already accumulated on the surface (note that the surface potential is shielded within a few Debye lengths above the surface). As a result, the charge-transfer rate changes depending on the surface charge. This process continues until the net current onto the surface becomes zero. In general, the surface charge will not be zero in the equilibrium state. For example, the surface equilibrium potential will be positive in regions where the photoelectron current dominates. Considering typical photoelectron temperatures of a few eV, a straightforward charging theory predicts slightly positive potentials of sunlit surfaces of less than +10 V. However, in the terrestrial magnetotail lobe, where the incident currents from the ambient plasma become very small, the surface potential can become much higher than expected from a simple current-balance model based on Maxwellian plasmas. In this region, the energy distribution of the photoelectrons has important implications for the surface potential. *Pedersen* [1995] suggested that a high-energy tail population in the photoelectron energy distribution causes the large positive spacecraft

[1]Department of Geophysics, Kyoto University, Kyoto, Japan.
[2]Space Sciences Laboratory, University of California, Berkeley, California, USA.

Corresponding author: Y. Harada, Department of Geophysics, Kyoto University, Oiwake-cho, Sakyo-ku, Kyoto 606-8502, Japan. (haraday@kugi.kyoto-u.ac.jp)

2169-9380/13/10.1002/jgra.50296

potentials of tens of volts detected in the Earth's magnetotail. The spacecraft surface potentials can reach approximately +70 V in the tail lobe [*Schmidt et al*., 1995].

[4] It is likely that spacecraft photoelectrons have high-energy tail populations, since dozens of spacecraft have observed large positive potentials in the tail lobe. On the other hand, the energy distribution of photoelectrons originating from the lunar surface remains unclear. *Reasoner and Burke* [1972] reported a Charged Particle Lunar Environment Experiment (CPLEE) observation of lunar photoelectrons that returned to the surface with energies of up to 200 eV. They explained the observed electron energy distribution and the inferred large positive potential of $\sim$ +200 V by assuming a constant photoelectron yield function for the high-energy tail of solar photons. However, this assumption is inconsistent with the experimental result from the returned lunar fines by *Feuerbacher et al.* [1972], who showed that the photoelectron yield drops off steeply for higher-energy incident photons after a peak at 14 eV. The calculated energy distribution under solar irradiation exhibits a mean energy of 2.2 eV and an extremely weak tail. At present, it is uncertain whether or not the photoelectron yield of the lunar surface remains high for high-energy incident solar photons. Information about the photoelectron energy distribution is crucial for determining how large the lunar surface potentials would be in the tail lobe.

[5] Although the Moon does not possess a thick atmosphere, it does have a tenuous, collisionless exosphere, composed of neutral particles of lunar origin [*Stern*, 1999]. Once a neutral particle has been ionized in the solar wind, the newborn ion will be accelerated by the convection electric field and eventually be "picked up" by the solar wind. Lunar pickup ions have been observed by several spacecraft in the solar wind [*Hilchenbach et al.*, 1993; *Mall et al.*, 1998; *Yokota et al.*, 2009; *Halekas et al.*, 2012]. Heavy ions of lunar origin have also been observed above the Moon's dayside in the terrestrial magnetotail lobe [*Tanaka et al.*, 2009; *Poppe et al.*, 2012a].

[6] Here we report Moon-related electron and ion signatures observed by ARTEMIS in the terrestrial magnetotail lobe. The ARTEMIS mission [*Angelopoulos*, 2011] conducts comprehensive plasma and wave observations by employing two probes that orbit the Moon. Using simultaneous observations by probes that are, respectively, near and distant from the Moon, we can separate Moon-related phenomena from those intrinsic to the ambient plasma. The ARTEMIS measurements of electron velocity distributions, utilizing knowledge of the spacecraft potential, enables us for the first time to quantitatively interpret the energy spectra of upward-traveling electrons that play the crucial role in the surface charging mechanisms. We first show the pitch angle and energy distributions of field-aligned, upward-traveling electrons from the dayside lunar surface and discuss their generation processes and implications for large positive potentials of the lunar surface. We then present dual-probe data on Moon-related populations observed above the Moon's dayside, which confirm the large positive surface potentials and indicate that plasma of lunar origin dominates the lobe plasma populations that are also present. In addition, we present modified electron-velocity distribution functions associated with Moon-related populations. These ARTEMIS observations reveal an interesting plasma environment, where dominant heavy ions are accelerated near the positively charged surface, expanding several hundreds of kilometers above the Moon's dayside and potentially interacting with the ambient-plasma populations.

2. Field-aligned, Upward-traveling Electrons From the Dayside Lunar Surface in the Tail Lobe

[7] We first present the ARTEMIS data of the field-aligned, upward-traveling electrons from the dayside lunar surface observed when the Moon is located in the terrestrial magnetotail lobe. Analysis of the pitch-angle and energy characteristics of the upward-traveling electrons provides important pieces of information about the near-surface dynamics of electrons, as well as on the electrostatic potentials of the dayside lunar surface. The surface potentials, which are mainly determined by electron dynamics, have significant implications for the near-surface dynamics of newborn ions of lunar exospheric origin.

[8] Figure 1 shows the ARTEMIS P2 lunar dayside observations in the terrestrial magnetotail on 7 January 2012, based on data from the ESA (electrostatic analyzer) [*McFadden et al.*, 2008a], EFI (electric field instrument) [*Bonnell et al.*, 2008], and FGM (fluxgate magnetometer) [*Auster et al.*, 2008] instruments. The orbits of the two probes and the average magnetic field direction during this time interval are shown in Figure 2. High-energy electrons and ions with energies greater than 1 keV were not observed, and the magnetic field data show a coherent, dominant, and positive B_x component, indicating that the Moon was located in the northern tail lobe. Straight-line magnetic field traces from the spacecraft imply a magnetic connection between the spacecraft and the dayside lunar surface at 17:55–18:25. As seen in the electron pitch angle distributions, a considerable flux of upward-traveling electrons with pitch angles between 0° and 90° was detected during this magnetically connected interval. The upward-traveling electrons exhibit a field-aligned signature, particularly near the beginning and end of the connected interval.

[9] The field-aligned signature of the upward-traveling electrons can be explained by considering electron emission from an extended surface in an oblique magnetic field, as sketched in Figure 3a. Electrons with pitch angles (α) smaller than the elevation angle (δ) of the magnetic field from the surface will be emitted with all 360° gyrophases, as shown by the red, complete cone. They will all travel upward along the field line without striking the surface, because their trajectories are spatially restricted within a cone of angle δ from the magnetic field (cf. the red trajectory in Figure 3b). On the other hand, the initial gyrophases of electrons with $\delta < \alpha < 90°$ are limited because of the presence of the surface, as shown by the blue, partial cone in Figure 3a. Some will strike the surface because of their gyromotion around the oblique field line (cf. the blue trajectory in Figure 3b). This shadowing effect of magnetized particles by an extended, absorbing surface, which is called "cyclotron shadowing" [*Reiff*, 1976] or the "gyroloss effect" [*Harada et al.*, 2010, 2012], depends on the initial gyrophase of the emitted electrons. This cyclotron shadowing further reduces the range of the emitted gyrophases with which electrons can travel upward to outer space along the magnetic field. Electrons emitted with $\alpha > 90°$ are unable

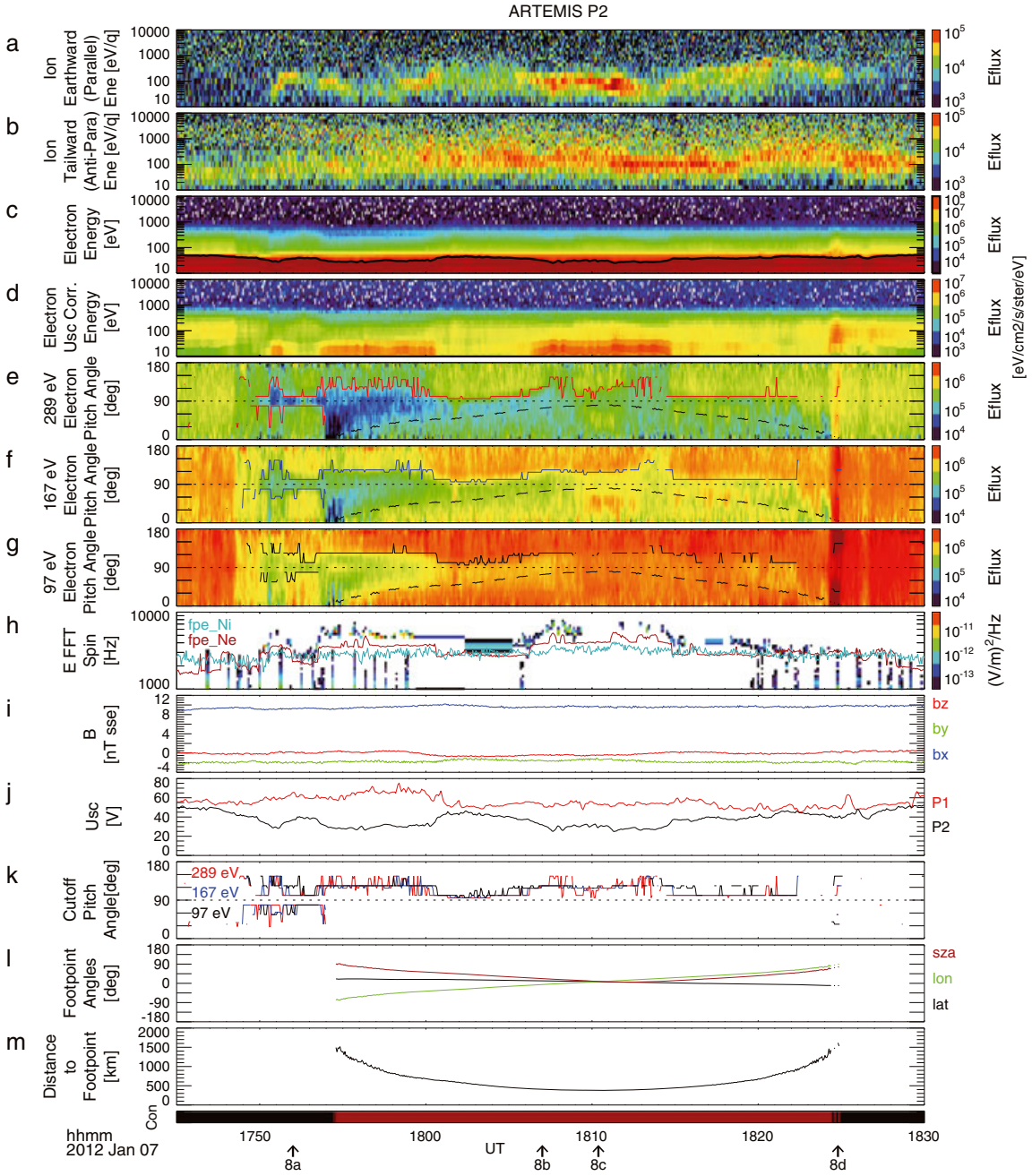

Figure 1. Time series data from an ARTEMIS P2 lunar-dayside flyby in the magnetotail lobe on 7 January 2012. Differential energy-flux spectra for ions with pitch angles of (a) 0–90° (earthward, corresponding to the upward motion from the Moon's dayside) and (b) 90–180° (tailward, corresponding to the downward motion toward the Moon's dayside), for omnidirectional electrons (c) with the spacecraft potential indicated by the black line and (d) with the spacecraft potential corrected, (e–g) electron pitch angle spectra for three energy channels, (h) high-frequency electric field spectra from the spin-plane sensors, (i) magnetic field in selenocentric solar ecliptic (SSE) coordinates, (j) spacecraft potentials from P2 and P1, (k) cutoff pitch angles derived from the electron pitch angle distribution averaged over three spin periods, (l) solar zenith angle, longitude, and latitude of the foot point, and (m) distance along the field line to the foot point. The dashed lines in Figures 1e–1g indicate the elevation angle δ of the magnetic field from the lunar surface estimated from straight-line magnetic field extrapolations. The red, blue, and black lines in Figures 1e, 1f, and 1g show the cutoff pitch angle at each energy corresponding to the lines in Figures 1k. The light-blue and red lines in Figure 1h show the electron plasma frequencies calculated from the moments of the observed ion and electron distributions, respectively. The bottom color bar indicates magnetic connection to the lunar surface in red and no connection in black. The four arrows below the time axis denote the timing at which the electron distributions shown in Figure 8 were obtained.

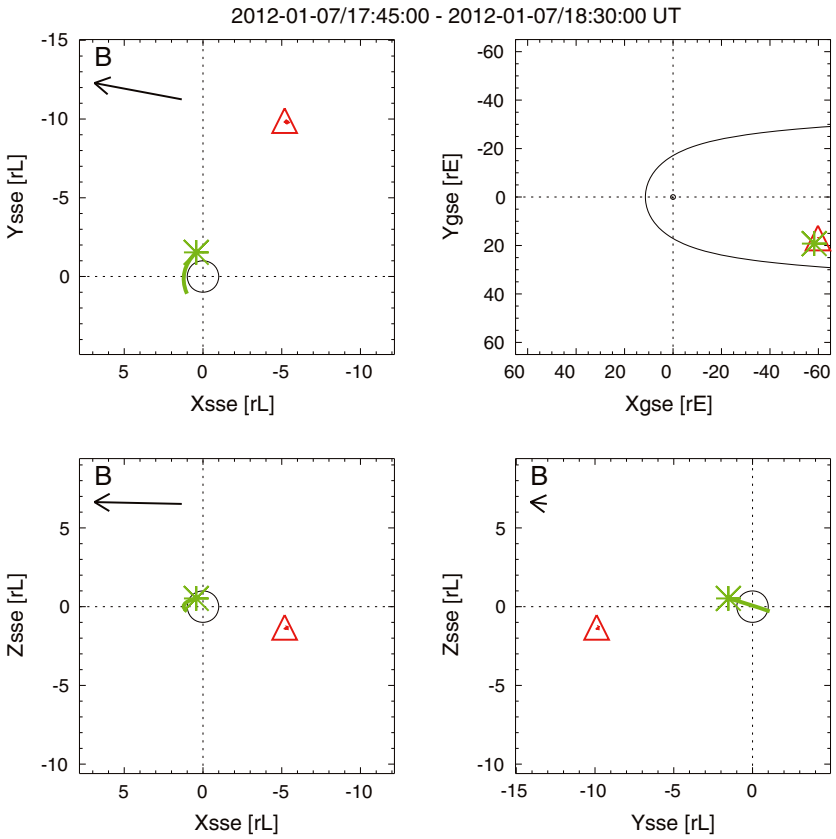

Figure 2. ARTEMIS P1 (red) and P2 (green) orbits for the event shown in Figures 1 and 5, with the initial locations indicated by the red triangles and the green asterisks, respectively (the lunar radius r_L = 1738 km and the Earth radius r_E = 6378 km). The selenocentric solar ecliptic (SSE) system has its X-axis from the Moon toward the Sun, the Z-axis is parallel to the upward normal to the Earth's ecliptic plane, and the Y completes the orthogonal coordinate set, whereas the geocentric solar ecliptic (GSE) system has its X-axis from the Earth toward the Sun. The black arrows show the magnetic field directions averaged over the orbits. The black line in the top right-hand panel shows the typical location of the magnetopause in GSE coordinates, indicating that the Moon was located in the magnetotail.

to travel upward along the field line. They will all return to the surface. Eventually, a boundary will appear at δ in the upward-traveling pitch angle distribution, where the oblique magnetic field starts to be effective in restricting the initial gyrophase (Figure 3c). For example, even if the electron emission is isotropic, the gyrophase-averaged electron flux at $\delta < \alpha < 90°$ will be reduced compared with the flux at $0° < \alpha < \delta$ because of both gyrophase-limited emission and cyclotron shadowing, resulting in a field-aligned signature of the upward-traveling electrons.

[10] We now compare the electron data with the prediction of the oblique magnetic field effect. We can estimate the magnetic-elevation angle δ from the straight-line magnetic field traces. First, the observed magnetic field vector is extrapolated from the spacecraft until the field line crosses the lunar surface. We then compute δ based on the geometry of the magnetic field vector relative to the surface normal at the foot point. The dashed lines overplotted on the electron pitch angle distributions in Figures 1e–1g indicate the estimated elevation angles δ. At each energy, a relatively large flux is observed for $0° < \alpha < \delta$, and the flux decreases for $\delta < \alpha < 90°$. The observed pitch angle distributions of the upward-traveling electrons are in good agreement with the theoretical prediction of the gyrophase-limited zone for $\delta < \alpha < 90°$, particularly at 17:55–18:00 and 18:20–18:25. This implies that the oblique magnetic field effect causes the field-aligned signature of the upward-traveling electrons.

[11] The agreement of the observed pitch angle distribution with the theoretical prediction seems to be indistinct at 18:00–18:20. There are several possible reasons why it is difficult to see the oblique magnetic field effect during this time period. First, if upward electrons include magnetically reflected populations, the reflected electrons with large flux will "mask" the smaller-flux electrons emitted from the lunar surface. The spot-like bright signatures seen in the upward-electron distributions at 18:02, 18:10–18:13, 18:15, 18:17, and 18:18 (Figures 1e–1g) are presumably due to the magnetic reflection. These features will be discussed in more detail in section 4. Second, electron emission from the lunar surface might not be isotropic. As δ approaches 90°, the electron shadowing becomes less effective. If the emitted-electron distribution is originally field-aligned, it will be difficult to identify the boundary at δ in the pitch angle distribution.

[12] Another interesting issue regarding the field-aligned, upward-traveling electrons from the dayside lunar surface in

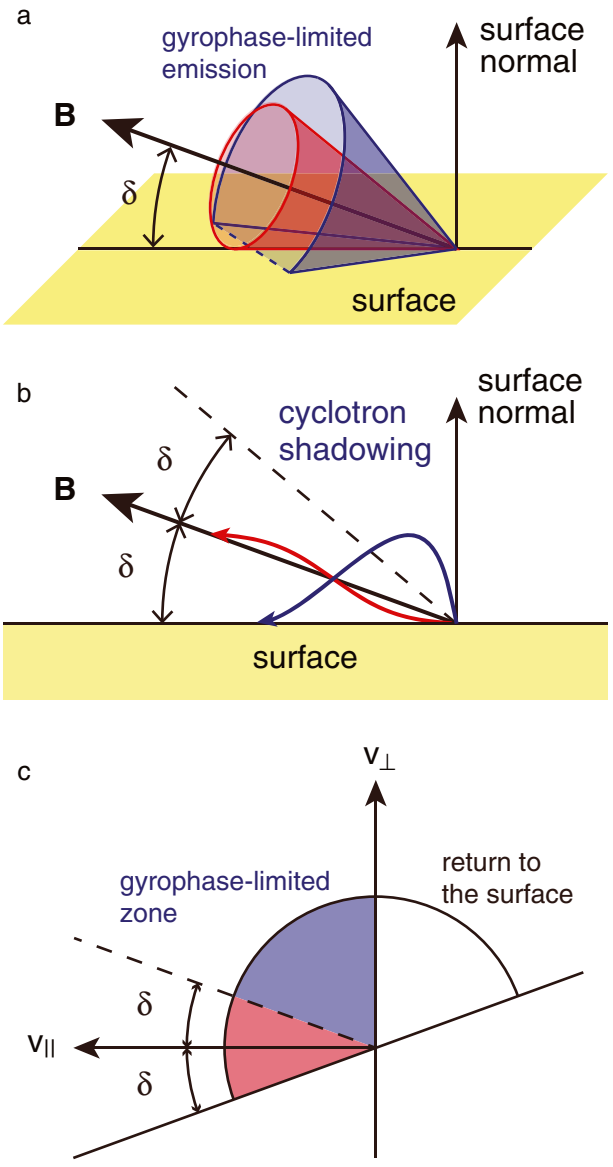

Figure 3. Schematic illustration of (a) electron emission from an extended surface in an oblique magnetic field, (b) cyclotron shadowing by the surface, and (c) the velocity distribution function of the emitted electrons.

the tail lobe relates to their energy distributions. Figure 4 shows the energy distributions of the field-aligned, upward- and downward-traveling electrons in the energy range < 200 eV obtained by P2 at 18:05–18:06. Figure 4b shows the electron-energy spectra corrected for the spacecraft potential from those shown in Figure 4a. One can see that large-flux spacecraft/instrument photoelectrons are successfully removed from the electron-energy spectra.

[13] Here we compare the upward- and downward-electron flux along the field line. If we assume that the electron distribution over the entire velocity space is obtained and ion currents are negligible, then the sum of the upward- and downward-electron currents should balance. The upward- and downward-flux along the field line, F_u and F_d, can be calculated as $F_u = \int\int J|\cos\alpha|d^2\Omega dE$ for $0° < \alpha < 90°$, and $F_d = \int\int J|\cos\alpha|d^2\Omega dE$ for $90° < \alpha < 180°$, where J is the differential flux, E is the energy, and Ω is the solid angle. We use the electron-energy spectrum from P2 at 18:05–18:06 corrected for the spacecraft potential in units of distribution function and convert it to differential flux. The integration over the available energy range and each hemisphere yields $F_u = 6.8 \times 10^6$ cm^{-2} s^{-1} and $F_d = 7.5 \times 10^6$ cm^{-2} s^{-1}. The integrated upward-electron flux is slightly smaller than the integrated downward-electron flux. The discrepancy can be attributed to the lowest-energy population that ESA cannot resolve and/or contribution from ion currents. For example, lack of observation of upward-traveling electrons with very low energies results in underestimation of F_u.

[14] In Figure 4b, the upward-traveling distribution indicated by the red line is much higher than the one-count level. The fact that the upward-traveling electrons still have such large populations, even with relatively high energies of ~10–200 eV, can constrain their source mechanisms. The dayside lunar surface mainly emits three types of electrons, i.e., photoelectrons, secondary electrons, and backscattered electrons. Incident electrons that are reflected by magnetic or electric fields before they strike the lunar surface may also exist. Generally, secondary electrons and core populations of photoelectrons are expected to be very cold, with a characteristic temperature of a few eV [*Whipple*, 1981]. These cold populations are inconsistent with the relatively hot energy distribution of upward-traveling electrons with energies of ~10–200 eV. Backscattering electrons, on the other hand, can be emitted with energies comparable to those of the incident electrons. However, the backscattering coefficient is usually expected to be less than 0.3 for ~100 eV incident electrons [*Whipple*, 1981]. This fraction is insufficient to explain the observed population significantly larger than 30% of the downward electrons (indicated by the dashed line in Figure 4b).

[15] Possible explanations for the upward-traveling electrons with energies of ~10–200 eV include (i) high-energy tail populations of lunar photoelectrons, (ii) incident electrons reflected by a nonmonotonic electrostatic-potential structure near the dayside lunar surface [*Poppe and Horanyi*, 2010; *Poppe et al.*, 2011, 2012b; *Halekas et al.*, 2011], and (iii) incident electrons adiabatically or nonadiabatically reflected by the remanent crustal magnetic fields [*Anderson et al.*, 1975; *Halekas et al.*, 2010]. We note that upward-traveling electrons with energies < 50 eV have a larger flux than incident electrons (Figure 4b). This excess population cannot be explained by any reflection processes which conserve particle energies, including electrostatic or magnetic reflection. Therefore, we suspect that at least the lower-energy population of the upward-traveling electrons with energies of ~10–50 eV mainly consists of high-energy photoelectrons after deceleration through a potential just above the dayside lunar surface.

[16] The presence of a large population of upward-traveling electrons with relatively high energies of ~10–200 eV has significant implications for the current balance on the lunar surface. In the tail lobe, the electron current from the ambient plasma is very small. Therefore, most upward-traveling electrons should return to the surface to maintain the current balance. The presence of a large population of upward-traveling high-energy electrons means that

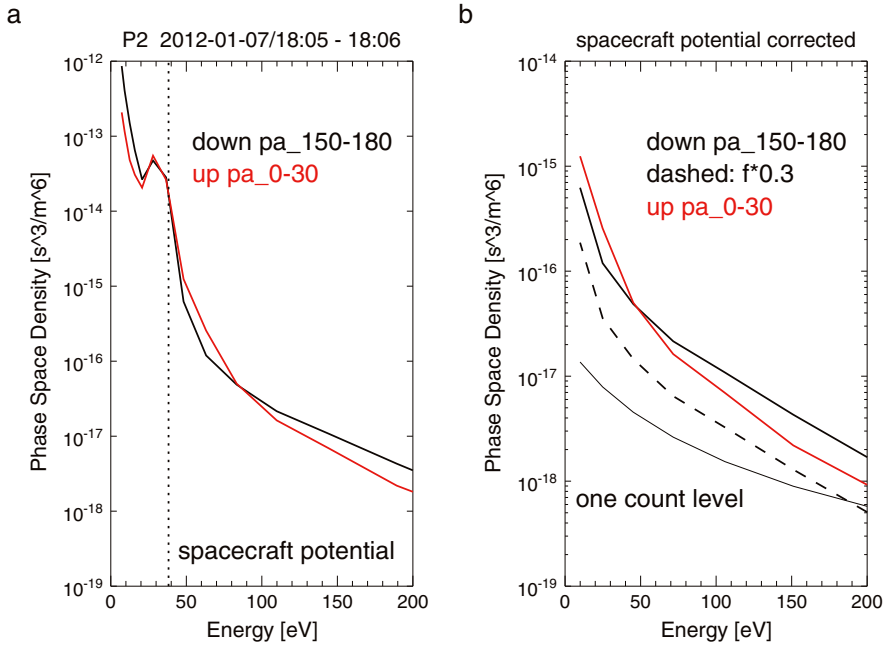

Figure 4. Electron-energy spectra in units of distribution function obtained by P2 at 18:05–18:06 UT on 7 January 2012. The black and red thick lines show electrons with pitch angles of 150–180° (downward) and 0–30° (upward), respectively. (a) The obtained energy spectra include contamination from spacecraft/instrument photoelectrons with energies lower than the spacecraft potential indicated by the vertical dotted line. (b) The spacecraft potential has been subtracted. It is seen that the spacecraft/instrument photoelectrons are successfully removed from the energy spectra. The dashed line shows 30% of the downward-traveling electron spectrum. The upward distribution of backscattered electrons is expected to be lower than this line. The black thin line indicates the one-count level.

large positive potentials are required to attract them back to the surface within the photoelectron sheath just above the surface and reach an equilibrium.

[17] The large positive potentials of the lunar surface will play an important role in the dynamics of newly ionized ions near the dayside lunar surface. These ions can interact with the lunar surface sheath in two ways: (1) Ions born within the sheath will gain acceleration from the surface field until they exit the sheath (where magnetotail convection then solely controls the ion motion), and (2) ions born near the Moon yet outside the lunar photoelectron sheath that are convected into the Moon by the magnetotail convection electric field can be repelled by the surface field and "scattered" along the magnetotail field lines. The strength of the lunar surface potential directly correlates to the energy that these ions can gain and in turn determines how far above the lunar surface the ions can travel before they are convected away by the geomagnetic field (A. R. Poppe et al., Model-based constraints on the lunar exosphere derived from ARTEMIS pick-up ion observations in the terrestrial magnetotail, submitted to *Journal of Geophysical Research*, 2013). In fact, Kaguya (at an altitude of 100 km) and ARTEMIS (at several hundred kilometers) have detected Moon-related ions which are presumably accelerated by the upward electric field caused by large positive potentials of the dayside lunar surface in the tail lobe [*Tanaka et al.*, 2009; *Poppe et al.*, 2012a]. We present a pickup-ion observation which supports the suggestion of large positive surface potentials in the next section.

3. Moon-Related Ions and Electrons Above the Dayside Lunar Surface in the Tail Lobe

[18] In this section, we compare the data from the dual-probe measurement on the lunar dayside and of ambient plasma, which indicate the existence of dominant ions and electrons of lunar origin with respect to the ambient-plasma populations in the tail lobe. The top two panels in Figures 1 and 5 show the earthward- (parallel to the magnetic field) and tailward-traveling (antiparallel) ions. These ion spectra from the two probes are also shown in Figure 6. P1 was located ∼10 lunar radii from the Moon (Figure 2) and detected tailward ions with energies of ∼100 eV, indicating a cold plasma flow from the Earth in the tail lobe (Figure 6e). Earthward-traveling ions were not detected by P1 (Figure 6d). On the other hand, P2 detected both earthward- and tailward-traveling ions above the lunar dayside (Figures 6a–6b). These earthward-moving ions detected by P2 travel upward from the Moon, suggesting a Moon-related origin.

[19] We now present more details of the ion-velocity distributions. The ion pitch angle distributions from the two probes are shown in Figures 6c and 6f. The Moon-related ions detected by P2 have different velocity components compared with the ambient ion flow detected by P1. The Moon-related ions have pitch angles between 0° and 90°, but not necessarily either 0° or 90°. These ions have both parallel and perpendicular velocity components [cf. *Poppe et al.*, 2012a], implying acceleration by parallel and perpendicular

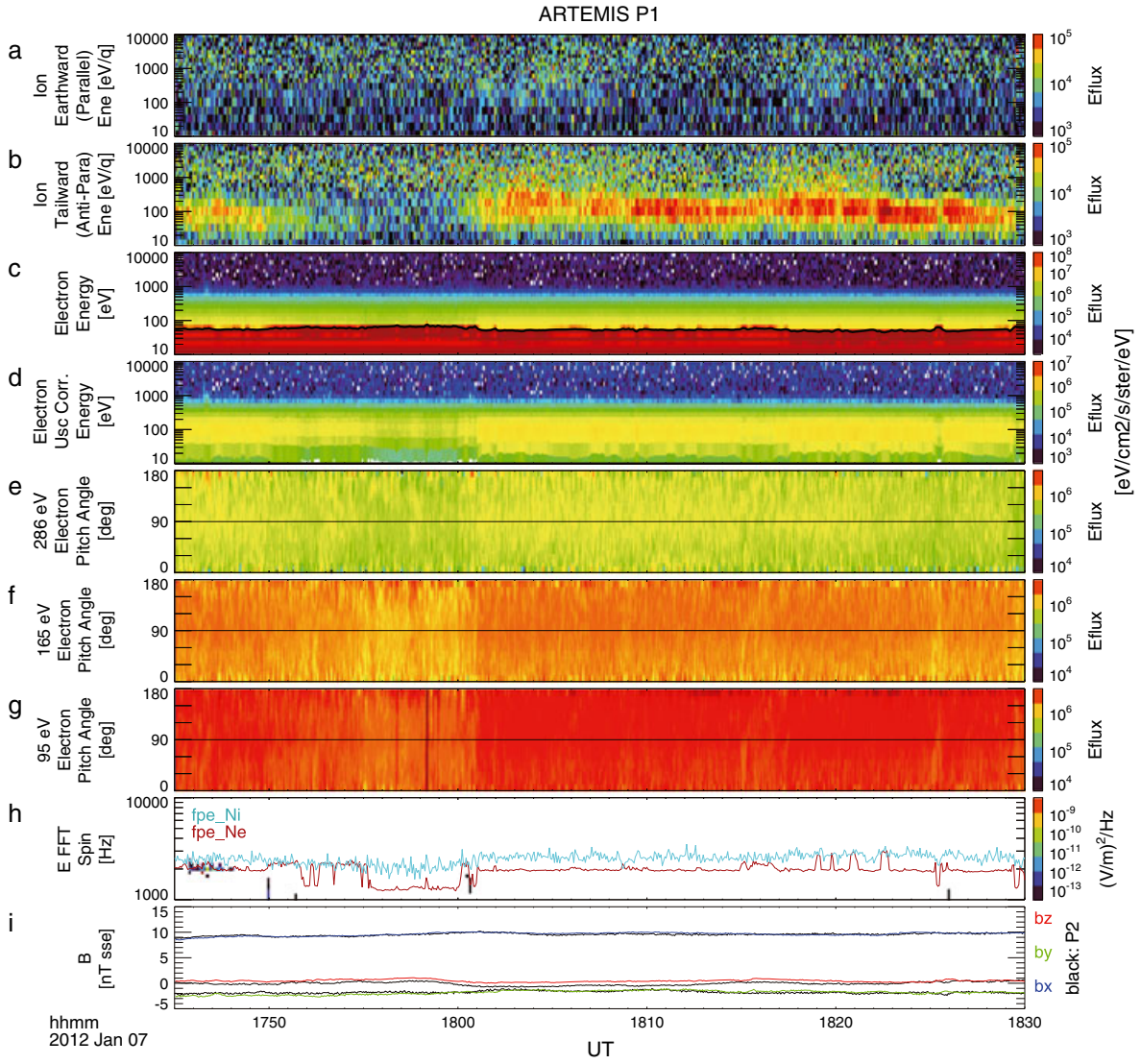

Figure 5. Time series data from ARTEMIS P1 during the same time interval as shown in Figures 1 and 2. All panels have the same format as Figures 1a–1i, except that the black lines in Figure 5i show the magnetic field data from ARTEMIS P2.

electric fields, such as by the lunar photoelectron sheath field (both parallel and perpendicular) and the magnetospheric convection electric field (only perpendicular). Considering the observed pickup-ion pitch angles of ∼60° and energies of ∼100 eV, and a spacecraft potential of ∼ +30 V at 18:11, we can estimate a lower limit to the positive lunar surface potential of ∼ +32.5 V by assuming that the near-surface electric field is oriented parallel to the magnetic field. We discussed the implications for large positive surface potentials in relation to the energy spectrum of the upward-traveling electrons in the previous section. They are consistent with the nonzero parallel-velocity component of the pickup ions deduced here. We note that it is possible to constrain the ion species from the energy and pitch angle spectra of pickup ions by assuming a reasonable convection speed, even though ARTEMIS probes are not capable of mass resolution [*Poppe et al.*, 2012a].

[20] Observations of the electron-plasma frequency, f_{pe}, can be used as a very useful diagnostic tool for the local electron density and also for the ion density on the assumption of charge neutrality. The electric field wave spectra from P2 show that the frequencies of the observed narrowband plasma oscillations, also known as Langmuir waves, occasionally rise up to well above the f_{pe} estimated from the moments of the observed ion distributions (Figure 1h). This implies the existence of missed low-energy ions that are repelled by the large positive spacecraft potential in the tail lobe, and/or of heavy ions. Since the density calculation is based on the "proton-only" assumption, the density fraction of heavy ions will be underestimated by a factor $\sqrt{M}$, where M is the ion-to-proton mass ratio [*McFadden et al.*, 2008b]. The detected frequencies are also higher than the f_{pe} estimated from the moments of the observed electron distributions. This is probably because the energy resolution around the spacecraft potential is not sufficiently high to resolve the enhanced cold electrons described below nor to derive an accurate density from the moment calculation. The detected frequencies go up to the highest detectable frequency of

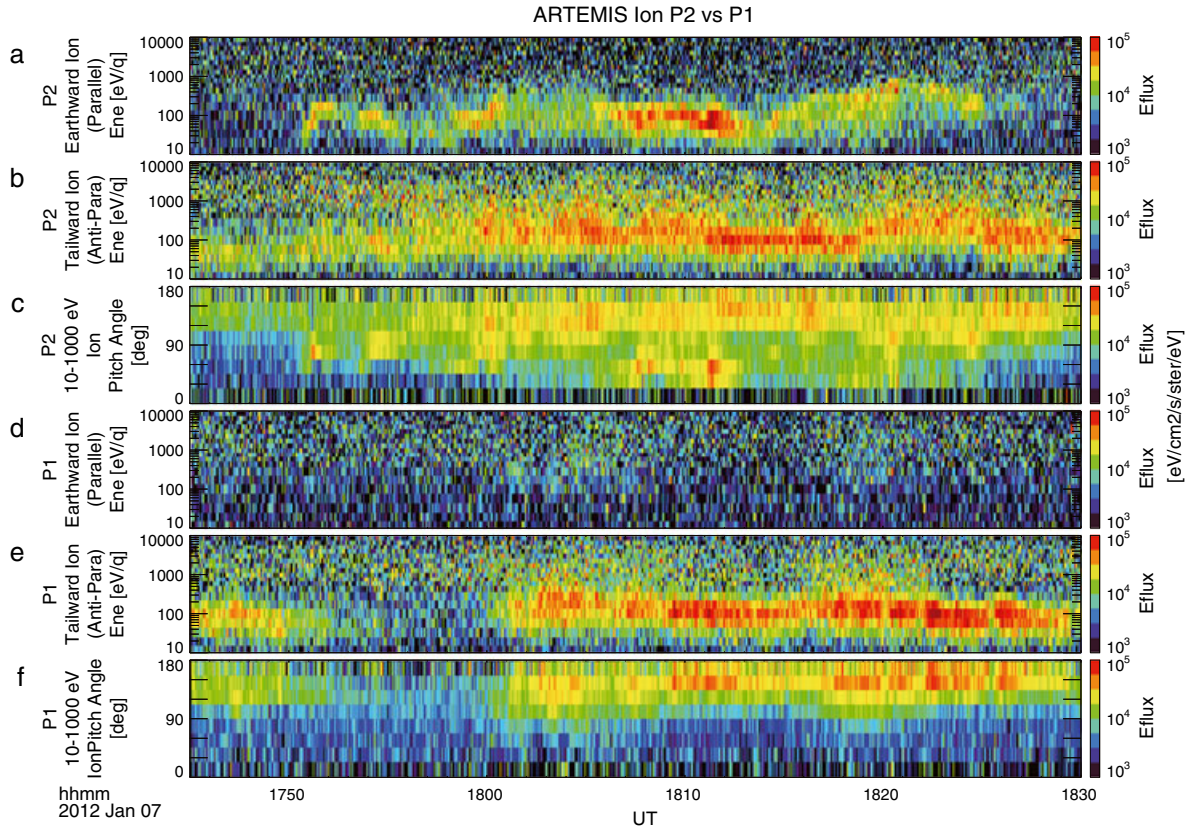

Figure 6. Time series data of ion energy and pitch angle spectra from ARTEMIS (a–c) P2 and (d–f) P1 during the same time interval as shown in Figure 1. Ion energy spectra in Figures 6a, 6b, 6d, and 6e are identical to those shown in Figures 1a, 1b, 5a, and 5b, respectively.

8 kHz at 18:08, implying a corresponding plasma density of $\sim$0.8 cm^{-3}. On the other hand, the electron-plasma frequencies detected and estimated by P1 remain < 4 kHz during the same time interval (Figure 5h). Thus, the P1 electric field and particle data indicate ambient-plasma densities of less than $\sim$0.2 cm^{-3}. The discrepancy between the plasma densities from the two probes implies the presence of several times as many ions and electrons above the lunar dayside as in the ambient plasma.

[21] The spacecraft potential provides another proxy for the plasma density. P2 detected a spacecraft potential decrease that was correlated with the plasma frequency's increase, whereas the P1 potential remained high (Figure 1j). This spacecraft potential reduction is presumably caused by an enhancement of the electron current incident onto the spacecraft, which is consistent with the density increase inferred from the plasma-wave observations.

[22] We also observe a Moon-related signature of cold electrons below 100 eV. Figure 7 shows a typical electron-energy spectra obtained by P2 at 18:10:23–18:10:27. We see characteristic spectra of photoelectrons emitted from the spacecraft surface and EFI probes in the energy range lower than the measured spacecraft potential. We can remove the spacecraft/instrument photoelectrons from the electron-energy spectra by subtracting the spacecraft potential from the electron energies. Figure 1d shows the electron energy-time spectrogram from P2, corrected for the spacecraft potential. We subtracted the spacecraft potential averaged over the spin from the energy spectrum in units of the distribution function and converted it to units of the differential energy flux when plotting the corrected energy spectrum. We observe a significant cold-electron enhancement at 17:50–17:52, 17:54–18:01, and 18:06–18:15. The electron data from P1, however, does not show a similar cold-electron enhancement (Figure 5d), suggesting that the cold electrons detected by P2 are related to the Moon. It is unlikely that the cold-electron enhancement include a significant amount of spacecraft/instrument photoelectrons, because the energy spectra of cold electrons just above the spacecraft potential are clearly different from those of the contaminating photoelectrons as shown in Figure 7. One simple interpretation of the Moon-related cold-electron enhancement is the appearance of newly ionized cold electrons of lunar exospheric origin.

[23] There seem to be good correlations among Moon-related signatures in the data from P2 described above; i.e., we simultaneously observe earthward-traveling ions, a spacecraft potential reduction, a cold-electron enhancement, and an increase in the electron-plasma frequency at 17:50–17:52, 17:54–18:01, and 18:06–18:15 (Figures 1a, 1d, 1h, and 1j). The correlations among these Moon-related signatures are consistent with an increase in the numbers of both electrons and ions ionized above the dayside lunar surface. As we have seen, the dual-probe ARTEMIS observation provides good evidence of the existence of Moon-related

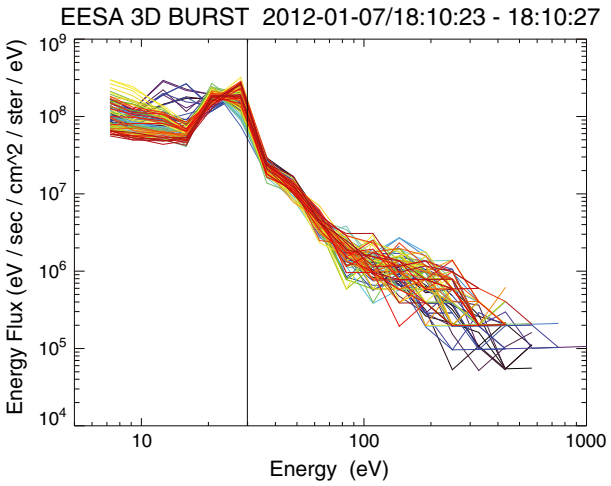

Figure 7. Electron-energy spectra in units of differential energy flux from ARTEMIS P2 at 18:10:23–18:10:27 UT. Each of the 88 solid angle bins are plotted separately. The vertical black line indicates the spin-averaged spacecraft potential of 30 V. Photoelectrons from the axial and radial EFI sensors are seen as the peaks at 12–16 eV and 28 eV, respectively [*McFadden et al.*, 2008a, cf. Figure 10]. The energy spectrum > 30 eV for each bin is clearly different from that of spacecraft/instrument photoelectrons with energies lower than the spacecraft potential, enabling the removal of the photoelectron contamination from the ambient-electron spectrum.

plasma with densities comparable to or even several times higher than the ambient density above the lunar dayside in the terrestrial magnetotail lobe.

4. Ambient Electron Modification Associated With Moon-related Populations

[24] Finally, we point out some interesting signatures in the electron-velocity distributions, which imply interactions between Moon-related plasma populations and ambient electrons of terrestrial and interplanetary origin. We observe a depletion in the omnidirectional electron flux at 17:48–17:55 when the field line is not connected to the Moon (Figures 1c and 1d). It is easier to see this flux depletion in the pitch angle spectrum panels because of their enhanced color scale (e.g., colors turning from red into yellow at 17:48 in Figure 1g). This overall flux depression during the unconnected interval might represent a convected flux tube that was partially emptied owing to lunar shadowing when it was connected to the Moon [*Anderson and Lin*, 1969; *Lin*, 1968; *McCoy et al.*, 1975]. In this case, the ARTEMIS P2 on the open field line in the tail lobe should observe earthward-electrons from the distant tail as soon as the flux tube is detached from the Moon. However, we do not see the earthward-electron flux ($\alpha < 90°$) larger than the tailward-electron flux ($\alpha > 90°$) in Figures 1e–1g. Meanwhile, another Moon-related phenomenon during the unconnected interval is observed; i.e., the spacecraft potential of P2 starts to decrease gradually at 17:48 (Figure 1j). We speculate that the Moon-related populations inferred from the spacecraft-potential reduction might be related to the flux depletion during the unconnected interval at 17:48–17:55, though we do not have any plausible explanation for its generation mechanisms yet.

[25] The electron pitch angle distributions from P2 show intermittent flux depletion around 90° at 17:50–18:22 (Figures 1e–1g). On the other hand, P1 detected almost isotropic electrons throughout this time interval (Figures 5e–5g), indicating that the 90° electron dropouts detected by P2 are Moon-related. The 90° dropouts appear on both the earthward ($\alpha < 90°$) and tailward ($\alpha > 90°$) sides at 17:50–17:55 when the spacecraft is not magnetically connected to the Moon. During the connected time, we see dropouts mainly in the incident electron distributions ($\alpha > 90°$), and sometimes in the upward electron distributions ($\alpha < 90°$). We find good correlations of the 90° electron dropouts with the Moon-related populations discussed in the previous section; i.e., we simultaneously observe the 90° electron dropouts and the signatures of Moon-related populations at 17:50–17:52, 17:54–18:01, and 18:06–18:15 (Figures 1a, 1d–1h, and 1j). This suggests direct or indirect interactions of ambient electrons with Moon-related populations.

[26] We also note an enhancement in counterstreaming electrons at 18:25 when the connected interval is just ending (Figures 1e–1g and the bottom color bar). This is a very special geometry, because the field line from the spacecraft passes very close to the Moon. In addition, we see Moon-related ions until 18:25 (Figure 1a). The combination of these unusual situations might be responsible for generating the counterstreaming electrons.

[27] We see spot-like bright signatures in the upward-traveling electron pitch angle distributions which have almost as high a flux as the incident electrons at 18:02, 18:10–18:13, 18:15, 18:17, and 18:18 (Figures 1e–1g). We presume that they are incident electrons that are magnetically reflected by the crustal fields. For example, the foot points at 18:10–18:13 are estimated at (latitude $\sim 6°$N, longitude $\sim 12°$E), where moderate crustal fields are inferred by *Halekas et al.* [2001]. They look like "conics" with flux peaks at intermediate pitch angles ($0° < \alpha < 90°$) rather than the loss-cone distributions expected from magnetic reflection of isotropic incident electrons.

[28] We look in more detail at the electron-velocity distributions when the Moon-related signatures are observed. Figure 8 shows $v_{\parallel}$–$v_{\perp}$ cuts of the electron-velocity distribution functions obtained at (a) 17:52:00–17:52:03, (b) 18:07:01–18:07:04, (c) 18:10:23–18:10:27, and (d) 18:24:48–18:24:52 (the observed timing is denoted by the arrows in Figure 1). As we saw in the pitch angle distributions, 90° dropouts are seen in (a) both earthward- and tailward-traveling electron populations, (b) downward-traveling electrons, and (c) both downward- and upward-traveling electrons, with large perpendicular velocities of > 5000 km s^{-1}. The flux depletion of hot electrons with all pitch angles in the positive parallel-velocity region (corresponding to upward electrons) in Figure 8b can be simply interpreted as due to hot-electron absorption by the lunar surface. The upward-traveling conic in Figure 8c can be interpreted as magnetically reflected anisotropic electrons; if the incident electrons are anisotropic with the 90° dropouts, then adiabatic reflection results in an upward-traveling conic. In Figure 8d, we observe counterstreaming

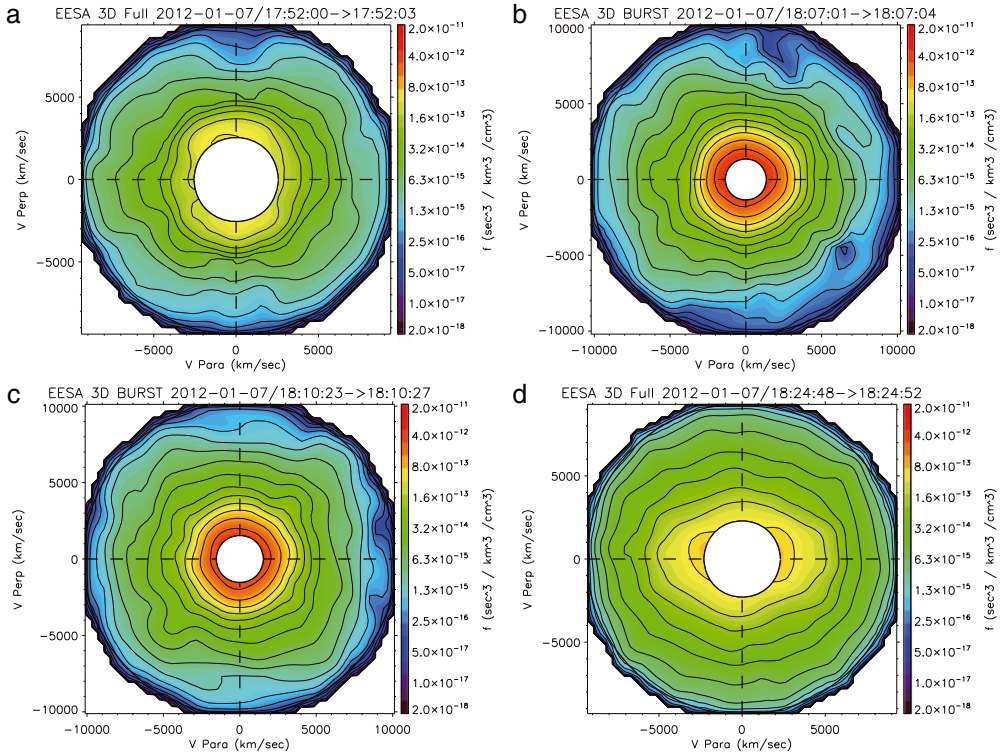

Figure 8. Electron distribution function slices from ARTEMIS P2 as a function of parallel and perpendicular velocity. Positive parallel velocity points earthward (corresponding to upward motion during the magnetically connected interval). The inner white circles indicate the lowest energies of the available data after subtraction of the spacecraft potential.

electrons enhanced along the field line without a clear signature of 90° hot-electron dropouts.

[29] Here we briefly discuss the angular distributions of the enhanced cold electrons. We see cold-electron enhancement in Figures 8a, 8b, and 8c. The enhanced cold electrons look anisotropic. However, we note that the angular distribution of the low-energy electrons cannot be trusted, since the spacecraft potential varies by several volts over the spin period as a result of the differential illumination of the EFI probes. If very cold electrons (e.g., newly ionized electrons of lunar exospheric origin) are present around the spacecraft, then they can be strongly modulated by this variable spacecraft potential, resulting in anisotropic enhancement of the lowest-energy electrons. We also note that the corrected energy spectra of the electrons shown in Figure 1d include some smearing effects, because we used the average spacecraft potential over the spin period to apply the correction.

[30] We now consider possible generation mechanisms for the 90° electron dropouts. To modify the electron-velocity distribution functions, we need electric or magnetic fields, or source/loss processes. As a way of removing the 90° electrons, we can consider collisions, wave-particle interactions ("microscopic" electric and magnetic fields), and large-scale electrostatic and magnetic structures ("macroscopic" electric and magnetic fields). However, our evaluation shows that the cross sections for collisions are too small for any reasonable density of target particles, such as neutral atoms and dust grains, to achieve the observed erosion of incident electrons. Typical cross sections of neutral atoms $\sigma_{en} < 10^{-19}$ m^2 [*Kieffer and Dunn*, 1966] and number densities near the surface $n_n < 10^6$ cm^{-3} [*Stern*, 1999] yield mean free paths $\lambda_{en} > 10^4$ km, which is much longer than the lunar radius (1738 km). The mean free path will increase rapidly, because the number density falls off exponentially as a function of altitude, and we would not expect that collisions with neutral atoms can take place sufficiently frequently to remove electrons. As for charged dust grains potentially levitating around the Moon [*Stubbs et al.*, 2006], if we assume that a dust particle with a radius $r_d \sim 0.1$ μm is charged to $\phi_d \sim +10$ V, then we can calculate its capacitance, $C \sim 4\pi\epsilon_0 r_d \sim 10^{-17}$ F [*Goertz*, 1989], and charge, $q = C\phi_d \sim 10^{-16}$ C. Considering Coulomb collisions, its cross section for 100 eV incident electrons is calculated as $\sigma_{ed} < 10^{-14}$ m^2. Using expected densities, n_d, of 10^{-5} to 10^{-6} cm^{-3} at 100–200 km altitude [*McCoy and Criswell*, 1974], the mean free path will be $\lambda_{ed} > 10^{10}$ km, which is again much longer than the size of the system. In addition, wave-particle interactions do not seem to occur, because we see no wave activity other than Langmuir waves in the electric and magnetic field data from P2 (not shown). Therefore, hereafter, we explore the possibility of the presence of large-scale electrostatic and magnetic structures.

[31] Both large-scale electrostatic and magnetic structures could produce 90° electron dropouts. If a field-aligned potential structure exists, as shown in Figure 9a, then incident electrons will be accelerated by the electric field along the magnetic field. Electrons with initially zero parallel-velocity component will have a parallel-velocity component of $\sqrt{2e\phi/m}$ after having been accelerated, where

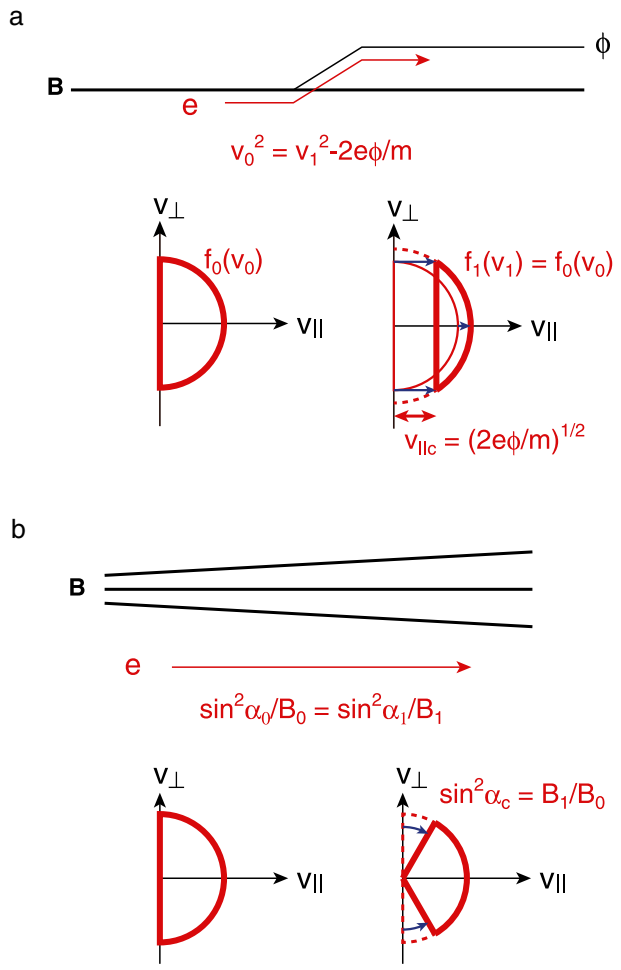

Figure 9. Schematic illustration of possible generation mechanisms of the 90° electron dropouts associated with (a) electrostatic acceleration along the magnetic field and (b) a pitch angle focusing effect owing to a nonuniform magnetic field configuration. The lunar surface and the spacecraft are located to the right along the magnetic field line. Initially isotropic downward-traveling electrons are modified by the time they reach the spacecraft. Note that the electrostatic process produces energy-dependent cutoff pitch angles, whereas the magnetic process results in energy-independent cutoff pitch angles.

e is the elementary charge, ϕ is the potential difference along the field line, and m is the electron mass. This results in a gap in velocity space with a constant cutoff parallel velocity $v_{\parallel c} = \sqrt{2e\phi/m}$. We note that the electrostatic potential we postulate here is not related to the lunar surface potential, because the surface potential should be shielded within a few Debye lengths, which is much smaller than the spacecraft altitude. On the other hand, if a nonuniform magnetic field configuration exists, as shown in Figure 9b, then conservation of the first invariant $\mu = mv_\perp^2/2B$ will render the pitch angles of the incident electrons smaller. This pitch angle focusing effect will also produce a gap in velocity space around $\alpha = 90°$, but with a constant cutoff pitch angle of $\alpha_c = \sin^{-1}\sqrt{B_1/B_0}$, where B_1 and B_0 are the magnetic field strengths at the spacecraft and in the upside region, respectively. Therefore, if an electrostatic process is responsible for the 90° dropouts, then the cutoff pitch angles will be energy-dependent, whereas the magnetic process will exhibit energy-independent cutoff pitch angles.

[32] We examine the energy dependence of the electron dropout angles around 90°. We define the cutoff pitch angle at each energy as the angle for which the slope of the electron pitch angle distribution, $s = \partial f/\partial\alpha$, becomes maximal for $90° < \alpha < 180°$ and minimal for $0° < \alpha < 90°$. We exclude upward-traveling electrons during the magnetically connected interval, adopt thresholds for the slope to get rid of flat isotropic distributions, and then plot the remaining cutoff pitch angles using red, blue, and black lines in Figures 1e–1g. The cutoff pitch angles for three energies are also plotted in Figure 1k. We see rapid fluctuations in the cutoff pitch angle for 289 eV, but the three cutoff pitch angles seem to behave in a similar fashion, suggesting that they are energy-independent. For field-aligned electrostatic acceleration with a constant cutoff parallel velocity, the cutoff pitch angles for different energies will obey a relationship of the form $\sqrt{E_1}\cos\alpha_{c1} = \sqrt{E_2}\cos\alpha_{c2}$, where α_{c1} and α_{c2} are the cutoff pitch angles for electron energies E_1 and E_2, respectively. This relationship is obviously not satisfied most of the time (cf. Figure 1k). Thus, the lack of energy dependence of the cutoff pitch angles implies a magnetic rather than an electrostatic origin of the 90° dropouts. We note, despite the implication of nonuniform magnetic fields suggested by the electron data, that the magnetic field data from the two probes indicate almost identical magnetic fields (Figure 5i). We will leave a detailed discussion of these enigmatic characteristics of the electron modification to a future investigation.

[33] As we have seen in this section, the ARTEMIS data exhibit very curious features of electron-velocity distribution functions associated with the Moon and plasma of lunar origin. Note that the incident electrons of terrestrial or interplanetary origin are already modified by the time they reach the spacecraft and the lunar surface. This means that the interaction region of ambient electrons and Moon-related populations extends at least several hundred kilometers above the Moon's dayside.

5. Conclusion

[34] We observe field-aligned, upward-traveling electrons from the dayside lunar surface when the Moon is located in the terrestrial magnetotail lobe. Their pitch angle distributions are in good agreement with the theoretical predictions of gyrophase-limited emission from an extended surface in an oblique magnetic field. The energy distributions of the upward-traveling electrons comprise a large population of over 100% of incident electrons with energies in the range ~10–50 eV and 30% with energies of ~50–200 eV. We speculate that at least the lower-energy population of the upward-traveling electrons primarily consist of the high-energy tail of photoelectrons emitted from the lunar surface. These new observations help resolve long-standing questions about the existence of large dayside surface positive potentials first inferred from Apollo CPLEE measurements. The large upward-traveling populations with relatively high energies of ~10–200 eV imply large positive potentials of the lunar surface. The large positive potentials will

accelerate a significant amount of newly ionized ions near the lunar surface, both parallel and perpendicular to the magnetic field, and play an important role in the plasma dynamics around the Moon in the tail lobe.

[35] The dual-probe ARTEMIS mission has revealed Moon-related signatures of ions and electrons in the tail lobe, which are only detected when the probe passes above the Moon's dayside. We simultaneously observe Moon-related ions, an increase in the electron plasma frequency, a spacecraft potential reduction, and a cold-electron enhancement. The Moon-related ions have both parallel- and perpendicular-velocity components. The nonzero parallel-velocity component of the pickup ions suggests large positive surface potentials of tens of volts, supporting the existence of a high-energy tail of lunar-surface photoelectrons. The electric-field wave spectra from the two probes show that the electron-plasma frequency rises above the Moon's dayside. A comparison of the electron-plasma frequencies between the two probes indicates the presence of several times as many ions and electrons above the lunar dayside as in the ambient plasma. The Moon-related spacecraft potential reduction indicates an enhancement of the electron current incident onto the spacecraft, which also implies that the electron density increases. The electron data show a cold-electron enhancement with energies below $\sim$100 eV, which suggests the existence of newly ionized cold electrons of lunar exospheric origin. The correlations among these Moon-related signatures are consistent with increases in the numbers of both electrons and ions ionized above the dayside lunar surface. Thus, the dual-probe ARTEMIS measurements confirm that plasma of lunar origin dominates the terrestrial and interplanetary plasma populations above the Moon's dayside in the tail lobe.

[36] The ARTEMIS data also exhibit modified electron-velocity distribution functions that correlate with the presence of Moon-related populations. The electron data show 90° electron dropouts, enhanced counterstreaming electrons, and upward-traveling conics. The upward-traveling electron conics can be explained as magnetically reflected anisotropic electrons with 90° dropouts. The good correlations between the 90° electron dropouts and the signatures of plasma of lunar origin imply direct or indirect interactions of ambient electrons with lunar pickup ions and electrons. The lack of energy dependence of the 90° dropouts implies a magnetic origin, whereas the magnetic field data from the two probes show almost identical magnetic fields. In future work, we will investigate in more detail the generation mechanisms of the 90° electron dropouts and counterstreaming electrons.

[37] The comprehensive observations of the lunar-dayside plasma environment in the tail lobe conducted by the dual-probe ARTEMIS mission provide us a wealth of information about Moon-related ion and electron populations and their interactions with the ambient plasma. We have seen that electrons and ions of both lunar and ambient origins are closely connected. Both the incident electron flux from the ambient plasma and the energy distribution of the upward-traveling electrons primarily decide the surface potential. The large positive surface potential, in turn, accelerates the dense newly ionized heavy ions outward from the Moon's dayside. These Moon-related ions potentially interact with the ambient plasma. In this environment, the heavy ions and cold electrons of lunar exospheric origin can predominantly exist in an ambient, low-β plasma which is characterized by a sub-Alfvénic convection flow. Further analysis of the ARTEMIS data, as well as theoretical work and numerical simulations, will be necessary for a complete understanding of the observed characteristics and of multiple-species plasma dynamics.

[38] **Acknowledgments.** We acknowledge NASA contract NAS5-02099 and V. Angelopoulos for use of data from the THEMIS Mission, J. W. Bonnell and F. S. Mozer for use of EFI data, and K. H. Glassmeier, U. Auster, and W. Baumjohann for use of FGM data provided under the lead of the Technical University of Braunschweig and with financial support through the German Ministry for the Economy and Technology and the German Center for Aviation and Space (DLR) under contract 50 OC 0302. This work was supported in part by a Research Fellowship for Young Scientists awarded by the Japan Society for the Promotion of Science.

[39] Masaki Fujimoto thanks the reviewers for their assistance in evaluating this paper.

References

Anderson, K. A., and R. P. Lin (1969), Observation of interplanetary field lines in the magnetotail, *J. Geophys. Res.*, *74*(16), 3953–3968, doi:10.1029/JA074i016p03953.

Anderson, K. A., R. P. Lin, R. E. McGuire, and J. E. McCoy (1975), Measurement of lunar and planetary magnetic fields by reflection of low energy electrons, *Space Sci. Instrum.*, *1*, 439–470.

Angelopoulos, V. (2011), The ARTEMIS mission, *Space Sci. Rev.*, *165*(1-4), 3–25, doi:10.1007/s11214-010-9687-2.

Auster, H. U., et al. (2008), The THEMIS fluxgate magnetometer, *Space Sci. Rev.*, *141*(1-4), 235–264, doi:10.1007/s11214-008-9365-9.

Bonnell, J. W., F. S. Mozer, G. T. Delory, A. J. Hull, R. E. Ergun, C. M. Cully, V. Angelopoulos, and P. R. Harvey (2008), The electric field instrument (EFI) for THEMIS, *Space Sci. Rev.*, *141*(1-4), 303–341, doi:10.1007/s11214-008-9469-2.

Feuerbacher, B., M. Anderegg, B. Fitton, L. D. Laude, R. F. Willis, and R. J. L. Grard (1972), Photoemission from lunar surface fines and the lunar photoelectron sheath, *Geochim. Cosmochim. Acta.*, *3*, 2655–2663.

Goertz, C. K. (1989), Dusty plasmas in the solar system, *Rev. Geophys.*, *27*(2), 271–292, doi:10.1029/RG027i002p00271.

Halekas, J. S., D. L. Mitchell, R. P. Lin, S. Frey, L. L. Hood, M. H. Acuña, and A. B. Binder (2001), Mapping of crustal magnetic anomalies on the lunar near side by the lunar prospector electron reflectometer, *J. Geophys. Res.*, *106*, 27,841–27,852.

Halekas, J. S., G. T. Delory, R. P. Lin, T. J. Stubbs, and W. M. Farrell (2008), Lunar prospector observations of the electrostatic potential of the lunar surface and its response to incident currents, *J. Geophys. Res.*, *113*, A09102, doi:10.1029/2008JA013194.

Halekas, J. S., R. J. Lillis, R. P. Lin, M. Manga, M. E. Purucker, and R. A. Carley (2010), How strong are lunar crustal magnetic fields at the surface?: Considerations from a reexamination of the electron reflectometry technique, *J. Geophys. Res.*, *115*, E03006, doi:10.1029/2009JE003516.

Halekas, J. S., G. T. Delory, W. M. Farrell, V. Angelopoulos, J. P. McFadden, J. W. Bonnell, M. O. Fillingim, and F. Plaschke (2011), First remote measurements of lunar surface charging from ARTEMIS: Evidence for nonmonotonic sheath potentials above the dayside surface, *J. Geophys. Res.*, *116*, A07103, doi:10.1029/2011JA016542.

Halekas, J. S., A. R. Poppe, G. T. Delory, M. Sarantos, W. M. Farrell, V. Angelopoulos, and J. P. McFadden (2012), Lunar pickup ions observed by ARTEMIS: Spatial and temporal distribution and constraints on species and source locations, *J. Geophys. Res.*, *117*, E06006, doi:10.1029/2012JE004107.

Harada, Y., et al. (2010), Interaction between terrestrial plasma sheet electrons and the lunar surface: SELENE (Kaguya) observations, *Geophys. Res. Lett.*, *37*, L19202, doi:10.1029/2010GL044574.

Harada, Y., et al. (2012), Nongyrotropic electron velocity distribution functions near the lunar surface, *J. Geophys. Res.*, *117*, A07220, doi:10.1029/2012JA017642.

Hilchenbach, M., D. Hovstadt, B. Klecker, and E. Möbius (1993), Observation of energetic lunar pick-up ions near Earth, *Adv. Space Res.*, *13*(10), 321–324.

Kieffer, L. J., and G. H. Dunn (1966), Electron impact ionization cross-section data for atoms, atomic ions, and diatomic molecules: I. Experimental data, *Rev. Mod. Phys.*, *38*, 1–35, doi:10.1103/RevModPhys.38.1.

Lin, R. P. (1968), Observations of lunar shadowing of energetic particles, *J. Geophys. Res.*, *73*, 3066–3071.

Mall, U., E. Kirsch, K. Cierpka, B. Wilken, A. Söding, F. Neubauer, G. Gloeckler, and A. Galvin (1998), Direct observation of lunar pick-up ions near the Moon, *Geophys. Res. Lett.*, *25*(20), 3799–3802, doi:10.1029/1998GL900003.

McCoy, J. E., and D. R. Criswell (1974), Evidence for a high altitude distribution of lunar dust, *Proc. Lunar Sci. Conf. 5th*, *5*, 2991–3005.

McCoy, J. E., R. P. Lin, R. E. McGuire, L. M. Chase, and K. A. Anderson (1975), Magnetotail electric fields observed from lunar orbit, *J. Geophys. Res.*, *80*, 3217–3224, doi:10.1029/JA080i022p03217.

McFadden, J. P., C. W. Carlson, D. Larson, M. Ludlam, R. Abiad, B. Elliott, P. Turin, M. Marckwordt, and V. Angelopoulos (2008a), The THEMIS ESA plasma instrument and in-flight calibration, *Space Sci. Rev.*, *141*(1-4), 277–302, doi:10.1007/s11214-008-9440-2.

McFadden, J. P., C. W. Carlson, D. Larson, J. Bonnell, F. Mozer, V. Angelopoulos, K. H. Glassmeier, and U. Auster (2008b), THEMIS ESA first science results and performance issues, *Space Sci. Rev.*, *141* (1-4), 477–508, doi:10.1007/s11214-008-9433-1.

Pedersen, A. (1995), Solar wind and magnetosphere plasma diagnostics by spacecraft electrostatic potential measurements, *Ann. Geophys.*, *13*(2), 118–129, doi:10.1007/s00585-995-0118-8.

Poppe, A., and M. Horanyi (2010), Simulations of the photoelectron sheath and dust levitation on the lunar surface, *J. Geophys. Res.*, *115*, A08106, doi:10.1029/2010JA015286.

Poppe, A., J. S. Halekas, and M. Horanyi (2011), Negative potentials above the day-side lunar surface in the terrestrial plasma sheet: Evidence of non-monotonic potentials, *Geophys. Res. Lett.*, *38*, L02103, doi:10.1029/2010GL046119.

Poppe, A. R., R. Samad, J. S. Halekas, M. Sarantos, G. T. Delory, W. M. Farrell, V. Angelopoulos, and J. P. McFadden (2012a), ARTEMIS observations of lunar pick-up ions in the terrestrial magnetotail lobes, *Geophys. Res. Lett.*, *39*, L17104, doi:10.1029/2012GL052909.

Poppe, A. R., J. S. Halekas, G. T. Delory, W. M. Farrell, V. Angelopoulos, J. P. McFadden, J. W. Bonnell, and R. E. Ergun (2012b), A comparison of ARTEMIS observations and particle-in-cell modeling of the lunar photoelectron sheath in the terrestrial magnetotail, *Geophys. Res. Lett.*, *39*, L01102, doi:10.1029/2011GL050321.

Reasoner, D. L., and W. J. Burke (1972), Characteristics of the lunar photoelectron layer in the geomagnetic tail, *J. Geophys. Res.*, *77*(34), 6671–6687, doi:10.1029/JA077i034p06671.

Reiff, P. H. (1976), Magnetic shadowing of charged particles by an extended surface, *J. Geophys. Res.*, *81*(19), 3423–3427, doi:10.1029/JA081i019p03423.

Schmidt, R., et al. (1995), Results from active spacecraft potential control on the geotail spacecraft, *J. Geophys. Res.*, *100*(A9), 17,253–17,259.

Stern, S. (1999), The lunar atmosphere: History, status, current problems, and context, *Rev. Geophys.*, *37*(4), 453–491, doi:10.1029/95JA01552.

Stubbs, T., R. Vondrak, and W. Farrell (2006), A dynamic fountain model for lunar dust, *Adv. Space Res.*, *37*(1), 59–66, doi:10.1029/1999RG900005.

Tanaka, T., et al. (2009), First in situ observation of the Moon-originating ions in the Earth's magnetosphere by MAP-PACE on SELENE (KAGUYA), *Geophys. Res. Lett.*, *36*, L22106, doi:10.1029/2009GL040682.

Whipple, E. C. (1981), Potentials of surfaces in space, *Rep. Prog. Phys.*, *44*, 1197–1250, doi:10.1029/2009GL040682.

Yokota, S., et al. (2009), First direct detection of ions originating from the Moon by MAP-PACE IMA onboard SELENE (KAGUYA), *Geophys. Res. Lett.*, *36*, L11201, doi:10.1029/2009GL038185.